

A Journal of the Gesellschaft Deutscher Chemiker

Angewandte Chemie

GDCh

International Edition

www.angewandte.org

Accepted Article

Title: Electronic Configuration Tuning of Centrally Extended Non-Fullerene Acceptors Enabling Organic Solar Cells with Efficiency Approaching 19%

Authors: Tainan Duan, Wanying Feng, Yulu Li, Zhixiang Li, Zhe Zhang, Huazhe Liang, Hongbin Chen, Cheng Zhong, Seonghun Jeong, Changduk Yang, Shanshan Chen, Shirong Lu, Oleg A. Rakitin, Chenxi Li, Xiangjian Wan, Bin Kan, and Yongsheng Chen

This manuscript has been accepted after peer review and appears as an Accepted Article online prior to editing, proofing, and formal publication of the final Version of Record (VoR). The VoR will be published online in Early View as soon as possible and may be different to this Accepted Article as a result of editing. Readers should obtain the VoR from the journal website shown below when it is published to ensure accuracy of information. The authors are responsible for the content of this Accepted Article.

To be cited as: *Angew. Chem. Int. Ed.* **2023**, e202308832

Link to VoR: <https://doi.org/10.1002/anie.202308832>

Electronic Configuration Tuning of Centrally Extended Non-Fullerene Acceptors Enabling Organic Solar Cells with Efficiency Approaching 19%

Tainan Duan^{a,d}, Wanying Feng^a, Yulu Li^d, Zhixiang Li^a, Zhe Zhang^a, Huazhe Liang^a, Hongbin Chen^a, Cheng Zhong^{c,*}, Seonghun Jeong^e, Changduk Yang^e, Shanshan Chen^f, Shirong Lu^d, Oleg A. Rakitin^g, Chenxi Li^a, Xiangjian Wan^a, Bin Kan^{b,*} and Yongsheng Chen^{a,*}

- [a] State Key Laboratory and Institute of Elemento-Organic Chemistry, The Centre of Nanoscale Science and Technology and Key Laboratory of Functional Polymer Materials, Renewable Energy Conversion and Storage Center (RECAST), College of Chemistry, Nankai University, Tianjin, 300071, China. E-mail: yschen99@nankai.edu.cn
- [b] School of Materials Science and Engineering, National Institute for Advanced Materials, Nankai University, Tianjin, 300350, China. E-mail: kanbin04@nankai.edu.cn
- [c] Hubei Key Laboratory on Organic and Polymeric Opto-electronic Materials, College of Chemistry and Molecular Sciences, Wuhan University, Wuhan, 430072, China. E-mail: zhongcheng@whu.edu.cn
- [d] Chongqing Institute of Green and Intelligent Technology, Chongqing School, University of Chinese Academy of Sciences (UCAS Chongqing), Chinese Academy of Sciences, Chongqing, 400714, China.
- [e] Department of Energy Engineering, School of Energy and Chemical Engineering, Perovtronics Research Center, Low Dimensional Carbon Materials Center, Ulsan National Institute of Science and Technology (UNIST), Ulsan 44919, Republic of Korea.
- [f] Key Laboratory of Low-grade Energy Utilization Technologies and Systems, CQU-NUS Renewable Energy Materials & Devices Joint Laboratory, School of Energy & Power Engineering, Chongqing University, Chongqing 400044, China.
- [g] N. D. Zelinsky Institute of Organic Chemistry Russian Academy of Sciences, 47 Leninsky Prospekt, Moscow, Russia.

Supporting information for this article is given via a link at the end of the document.

Abstract: In the molecular optimizations of non-fullerene acceptors (NFAs), extending the central core can tune the energy levels, reduce nonradiative energy loss, enhance the intramolecular (donor–acceptor and acceptor–acceptor) packing, facilitate the charge transport, and improve device performance. In this study, a new strategy was employed to synthesize acceptors featuring conjugation-extended electron-deficient cores. Among these, the acceptor CH-BBQ, embedded with benzobisthiadiazole, exhibited an optimal fibrillar network morphology, enhanced crystallinity, and improved charge generation/transport in blend films, leading to a power conversion efficiency of 18.94% for CH-BBQ-based ternary organic solar cells (OSCs; 18.19% for binary OSCs) owing to its delicate structure design and electronic configuration tuning. Both experimental and theoretical approaches were used to systematically investigate the influence of the central electron-deficient core on the properties of the acceptor and device performance. The electron-deficient core modulation paves a new pathway in the molecular engineering of NFAs, propelling relevant research forward.

Introduction

Organic solar cells (OSCs) are gaining considerable attention for being environmentally friendly, solution-processable, and their flexibility^[1]. In recent years, the revolutionary Y-series non-fullerene acceptors (NFAs) have emerged, featuring a unique electron-deficient unit-centered polycyclic core and electron-deficient flanks, leading to a remarkable surge in power conversion efficiencies (PCEs) of OSCs^[2]. State-of-the-art polymer donor/NFA binary systems have already achieved PCEs over 19% in single-junction OSCs^[3]. Compared to previously reported NFA derivatives like ITIC^[4], the Y-series NFAs exhibit highly efficient charge generation with minimal driving force and essentially reduced energy loss (E_{loss})^[5]. Moreover, they enable

panchromatic light harvesting across the ultraviolet (UV)–visible (vis) to near infrared (NIR) region, ensuring satisfactory photocurrent density in corresponding OSC devices^[6].

Numerous characterizations have been conducted to investigate the exceptional performance of Y-series NFAs. Single crystal X-ray diffraction revealed that Y-series acceptors can form a unique three-dimensional (3D) interpenetrated network through intermolecular π – π stacking^[7]. Unlike previously reported acceptor–donor–acceptor (A–D–A) structured NFAs, where charge transport relies on the pathway formed through π – π stacking between indanone terminal groups^[8], the introduction of the benzothiadiazole core in Y-series NFAs generates an unprecedented “end unit to central core” packing mode in addition to the original “end unit to end unit” mode^[2c]. This unique 3D intermolecular packing network facilitates efficient charge separation/transport, accelerates photon-to-electron conversion, suppresses charge recombination, and minimizes E_{loss} while retaining high PCE. Density functional theory (DFT) calculations^[9] further indicated that the benzothiadiazole-centered structure of Y-series NFAs grants them unique advantages, such as an enhanced quadrupole moment (Q_{π} , along the π – π stacking direction), which can provide a gradual change of electrostatic potential induced by charge–quadrupole interactions, leading to optimized morphology and barrierless charge generation in bulk-heterojunctions (BHJs)^[10].

The importance of the central core in high-performance NFAs has sparked interest in targeted modifications^[5a, 11]. Recently, our group reported central core extensions to develop high-performance NFAs (CH-series). Using a 3-step “reduction–oxidation–condensation” tandem reaction, the benzothiazole unit of Y-series NFAs can be converted to a π -extended phenazine core (Figures 2 and S1). This central core conjugation extension resulted in a multimodal and strong 3D intermolecular packing for CH-6^[2a]. As a result, charge transport in blend films improved,

radiative recombination with high luminescence efficiency was achieved, and nonradiative recombination loss was alleviated, leading to reduced energetic disorder in blend films compared to Y6. Consequently, a PCE of 18.33% and an open-circuit voltage (V_{OC}) of 0.89 V were achieved. Similarly, Wei's group developed an NFA called Qx-2, containing a dibenzophenazine core^[12]. Qx-2-based devices exhibited drastically reduced E_{loss} from improved exciton dissociation and alleviated nonradiative recombination, resulting in a record-high V_{OC} of 0.93 V and a PCE of 18.3%. These inspiring results indicate the great potential of breaking the PCE bottleneck of OSCs through molecular engineering, especially using the central core conjugation extension strategy mentioned above (Figure S1).

The preliminary results verified the effectiveness of the central core conjugation extension strategy in designing high-performance acceptors. However, several crucial questions remain unanswered. For example, the impact of fusing electron-deficient units (e.g., benzothiadiazole) on photovoltaic performance is yet to be explored, as most cases involved electron-rich unit fusion (phenyl, anthracene, etc.). Additionally, the influence of the electron configuration of the central core on photovoltaic performance requires further investigation. Bearing these questions in mind, we emphasize the necessity and importance of utilizing new designs for thorough exploration, thereby expanding the application scope of this new strategy.

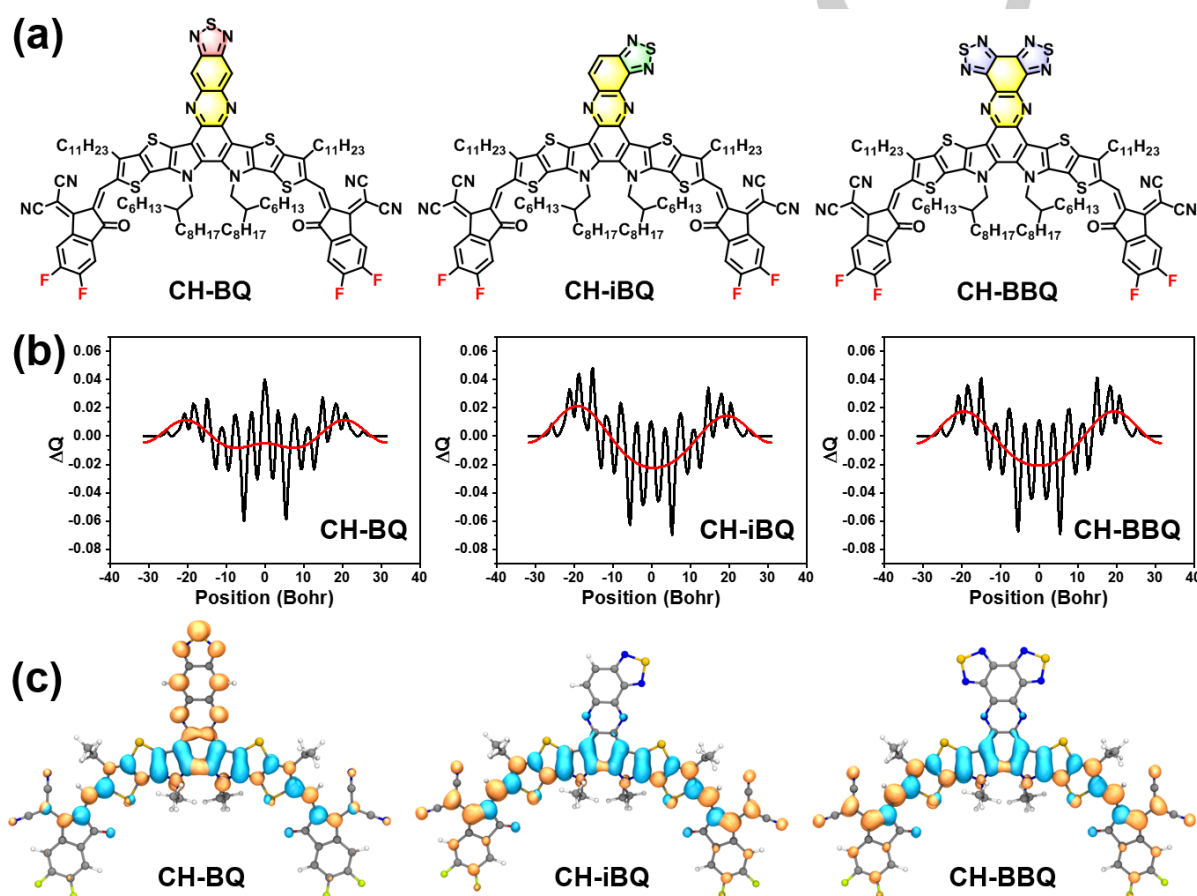


Figure 1. a) Molecular structures of acceptors. b) Theoretical density distribution ΔQ ($\Delta Q = \psi_{LUMO}^2 - \psi_{HOMO}^2$) along the longest axis (backbone) of acceptors. c) Hole (blue)–electron (yellow) distribution of acceptors calculated at relaxed S1 state.

In this contribution, three A–D–A featured NFAs (CH-BQ, CH-iBQ, and CH-BBQ) were constructed with different electron-deficient cores (Figure 1a). The two isomeric thiadiazole decorated NFAs, CH-BQ and CH-iBQ, differ only in the conjugate extension direction of the central core, while CH-BBQ features the benzobisthiadiazole-embedded structure. Compared to CH-BQ, CH-iBQ demonstrated optimized energy levels, better charge transport, and improved miscibility with the polymer donor (PM6). Consequently, PM6:CH-iBQ binary OSCs achieved a PCE of 17.97% with a V_{OC} of 0.875 V, a short-circuit photocurrent density (J_{SC}) of 26.04 mA·cm⁻², and an excellent fill factor (FF) of 78.5%. In contrast, PM6:CH-BQ-based devices demonstrated an inferior

PCE of 12.85%, V_{OC} of 0.84 V, J_{SC} of 23.61 mA·cm⁻², and a low FF of 64.8%. The benzobisthiadiazole-embedded acceptor, CH-BBQ, exhibited optimal fibrillar network morphology, improved charge generation/transport in blend films, leading to a PCE of 18.19% for PM6:CH-BBQ binary OSCs, and a further enhanced PCE of 18.94% for PM6:CH-BBQ:BO-4Cl ternary OSCs. To further understand the impact of electron-deficient core extension on the acceptors, donor/acceptor interactions, and photovoltaic device performance, DFT calculations and molecular dynamic (MD) simulation^[13] were performed. This work paves a new pathway for structure modifications and electronic configuration

tuning of NFAs, offering new guidelines for the molecular engineering of high-performance organic photovoltaic materials.

Results and Discussion

Before materializing the new NFAs, several basic DFT calculations were conducted to envision their properties. The A–D–A feature of the acceptors was examined using the characteristic peak-valley-peak plots, revealing their frontier orbital charge density differences (ΔQ) on the molecular backbone in the longest direction (Figure 1b). Surprisingly, while CH-iBQ and CH-BBQ exhibited polarized electron distribution and typical A–D–A feature, CH-BQ showed a more uniform electron distribution, potentially unfavorable for exciton separation, charge transport, and thus suppressing OSC performance compared to its counterparts^[14]. Meanwhile, the vertically extended CH-BQ

exhibited a high-lying highest occupied molecular orbital (HOMO) energy level, downshifted lowest unoccupied molecular orbital (LUMO), and consequently a reduced bandgap, distinct from its isomer CH-iBQ with horizontally extended core. The electron density distributions of HOMOs and LUMOs of CH-iBQ and CH-BBQ revealed a notable difference, while their electron-deficient cores barely participated in HOMO/LUMO delocalization and CH-BQ displayed the opposite behavior (Figure S3). This is also reconfirmed by the calculated hole–electron distribution at the relaxed S1 state (Figure 1c), indicating that the electron tends to be trapped in the extended central core in CH-BQ instead of shifting to its terminal groups. This anomaly resulted in a considerable overlap of hole/electron distribution for CH-BQ, potentially causing substantial variations in charge separation/recombination behavior compared to CH-iBQ and CH-BBQ^[15]. These calculated results spurred us to realize these molecules and investigate them experimentally.

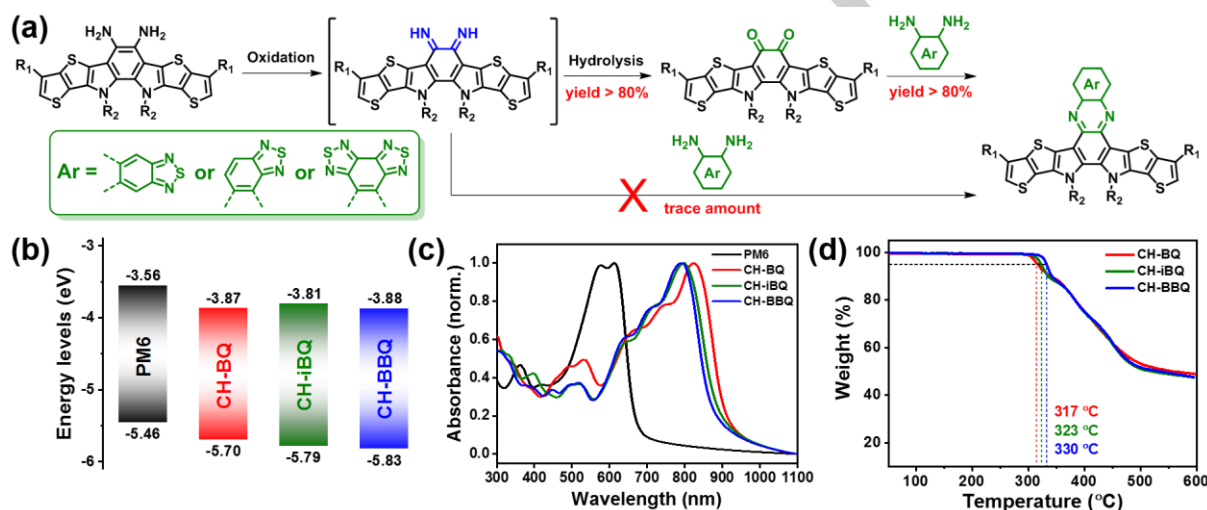


Figure 2. a) Synthetic route of the key π -conjugated backbones. b) Energy level diagram of PM6 and acceptors. c) Normalized absorption spectra of PM6 and acceptors. d) thermal gravimetric analysis curves of acceptors.

The synthetic procedure for the new acceptors is depicted in Figure 2a and Scheme S1. Initially, our previously developed di-imine intermediated method was adopted to synthesize three ring-fused cores, and three vicinal diamines were prepared according to the literature^[2a, 16]. However, the yield of the condensation reaction is almost negligible, probably owing to the reduced reactivity of three diamines induced by their electron-deficient unit. Using the commonly used “diamine-diketone” ring-closure condensation reaction, we successfully converted the diamines into the diketone via a 2-step “oxidation–hydrolysis” reaction. Subsequently, three target ring-fused cores were synthesized in good yield. Notably, the diketone compound was very stable and could be synthesized and stored on a large scale, streamlining the subsequent access. After obtaining the core units, acetylation and the Knoevenagel condensation reaction were conducted, leading to three final products (CH-BQ, CH-iBQ and CH-BBQ). This new synthetic method, complements our previously developed one and would facilitate versatile structure modification of NFAs.

To determine the energy levels of new acceptors, their electrochemical behaviors were investigated using cyclic

voltammetry (CV) (Figure S7). Compared to axisymmetric CH-BQ, CH-iBQ exhibited a downshifted HOMO (−5.70 eV vs. −5.79 eV), uplifted LUMO energy levels (−3.87 eV vs. −3.81 eV), and a widened bandgap, consistent with DFT calculations, as shown in Figure 2b. The vertically fused benzothiadiazole in CH-BQ enhanced its quinoidal character, explaining the energy level differences with the axisymmetric CH-iBQ, which can be explained with annellation theory, further discussed below. Furthermore, the HOMO/LUMO energy levels of CH-BBQ were further deepened (−5.83 eV/−3.88 eV) owing to an extra electron-deficient thiadiazole moiety. UV–vis spectroscopy investigated the photophysical properties of three acceptors. As shown in Figures 2c and S8, CH-BQ exhibited maximum absorption peaks located at 761 and 824 nm in dilute chloroform solution and neat film, respectively, with an $E_{\text{gap}}^{\text{opt}}$ of ~1.37 eV. Accordant with the CV results, CH-iBQ and CH-BBQ exhibited sequentially blue-shifted absorption profiles, with $E_{\text{gap}}^{\text{opt}}$ of ~1.39 and 1.42 eV, respectively. Interestingly, CH-BBQ exhibited the largest redshift ($\Delta\lambda$) of 71 nm (63 nm for CH-BQ and 66 nm for CH-iBQ) when transforming from solution to film, suggesting that its optimized intermolecular π – π stacking^[17]. The detailed physicochemical parameters are

summarized in Table S5. Additionally, using different ways of extending the electron-deficient core, the resulting acceptors exhibited varying thermal stability with decomposition

temperatures ranging from 317 °C to 330 °C, as measured by thermal gravimetric analysis (Figure 2d).

Table 1. Photovoltaic performance parameters of best devices based on CH-BQ, CH-iBQ, and CH-BBQ (PM6 as the polymer donor).

BHJs ^[a]	V_{oc} (V)	J_{sc} (mA/cm ²)	Calc. J_{sc} ^[b] (mA/cm ²)	FF (%)	PCE (%)
PM6/CH-BQ	0.840 (0.847±0.007)	23.61 (23.36±0.39)	22.65	64.8 (62.9±0.9)	12.85 (12.46±0.20)
PM6/CH-iBQ	0.879 (0.875±0.005)	26.04 (26.18±0.22)	25.13	78.5 (77.9±0.5)	17.97 (17.84±0.11)
PM6/CH-BBQ	0.881 (0.877±0.003)	26.15 (26.12±0.26)	25.21	78.9 (78.8±0.3)	18.19 (18.04±0.12)
PM6/CH-BBQ/BO-4Cl	0.882 (0.880±0.001)	27.05 (27.02±0.07)	26.20	79.4 (79.0±0.2)	18.94 (18.79±0.07)

[a] Statistical and optimal results are listed in parentheses and outside of parentheses, respectively. The average parameters were calculated from 8 independent devices. [b] Current densities calculated from external quantum efficiency curves.

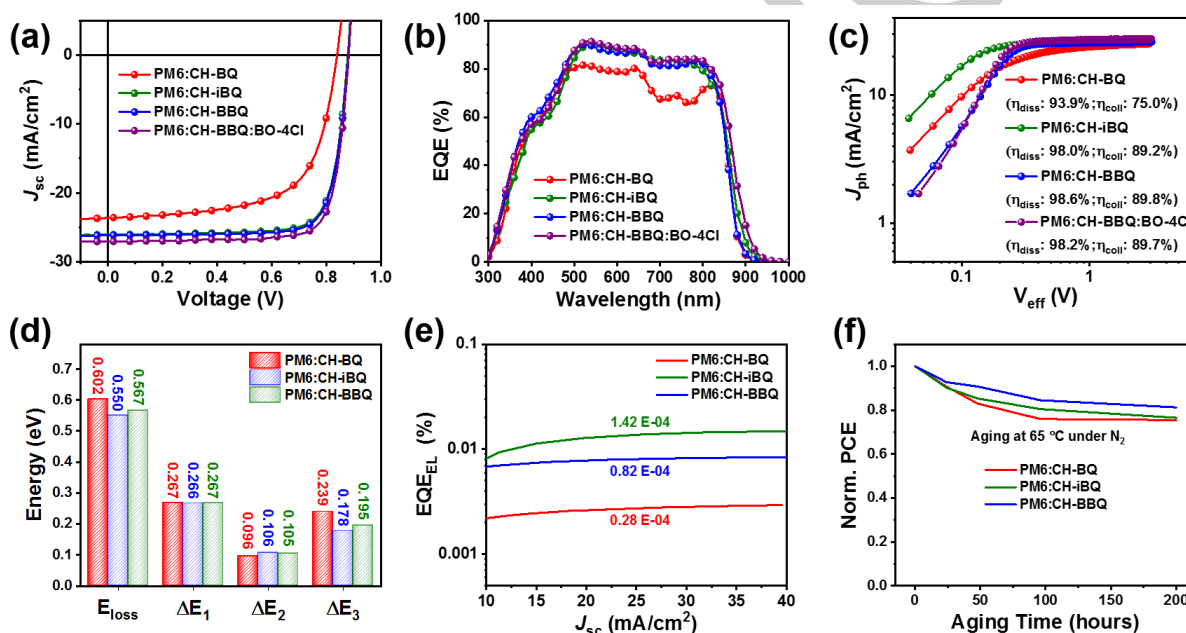


Figure 3. a) Current density–voltage (J - V) characteristics and b) external quantum efficiency curves of the optimized devices. c) Exciton dissociation/charge collection efficiencies of the optimized devices. e) The EQE_{EL} spectra for the optimized devices. d) E_{loss} diagram for the optimized devices. f) Thermal stability measurement for the optimized devices.

To evaluate how variations in the central electron-deficient core affect the photovoltaic performance of NFAs, OSCs were fabricated and characterized. PM6 was used as the polymer donor, and the conventional device architecture of ITO/PEDOT:PSS/active blend/PNDIT-F3N/Ag was adopted. OSC measurements were conducted under simulated solar illumination of AM 1.5G within a nitrogen-filled glovebox. Among the three NFAs, CH-BQ-based OSCs afforded the lowest J_{sc} of 23.61 mA·cm⁻², the lowest V_{oc} of 0.84 V, which is partially attributed to its deepened LUMO energy level, the minimum FF of 64.8%, and a mediocre PCE of 12.85% (Table 1). In contrast, the isomer of CH-BQ, CH-iBQ demonstrated excellent performance, achieving an improved PCE of 17.97% along with a V_{oc} of 0.879 V, J_{sc} of 26.04 mA·cm⁻², and FF of 78.5%. Notably, CH-iBQ-based OSCs achieved nearly 40% higher PCE compared to CH-BQ, contributing to its simultaneously improved V_{oc} , J_{sc} , and FF. A PCE record of 18.19% was achieved with CH-BBQ-based OSCs along with a V_{oc} of 0.881 V, J_{sc} of 26.15 mA·cm⁻², and FF

of 78.9%. Although the largest bandgap of CH-BBQ renders the narrow range of external quantum efficiencies (EQEs) spectra, (Figure 2b), its considerably high EQE values, especially in short-wavelength regions, guaranteed its superior J_{sc} and PCE. Moreover, by introducing a second NFA BO-4Cl into the PM6:CH-BBQ blend to construct ternary OSCs, the J_{sc} experienced another enhancement, leading to a PCE of 18.94% with V_{oc} of 0.882 V, J_{sc} of 27.05 mA·cm⁻², and FF of 79.4%.

To investigate the influence of electron-deficient core on the E_{loss} of OSCs, the total E_{loss} for three binary OSCs was analyzed using the following equation^[18]: $E_{loss} = E_g^{pv} - qV_{oc} = (E_g^{pv} - qV_{oc}^{60}) + (qV_{oc}^{60} - qV_{oc}^{ad}) + (qV_{oc}^{ad} - qV_{oc}) = \Delta E_1 + \Delta E_2 + \Delta E_3$. Here, E_g^{pv} represents the bandgap of the blend film, estimated via the derivatives of the sensitive EQE (EQE_{PV}) spectra, and q stands for the elementary charge. In this equation, ΔE_1 represents the unavoidable radiative loss originating from absorption above the bandgap, and V_{oc}^{SQ} is the maximum voltage based on the Shockley–Queisser (SQ) limit^[19]; ΔE_2 accounts for the radiative

energy loss caused by absorption below the bandgap, and the V_{OC}^{rad} is the V_{OC} when only radiative recombination occurs; ΔE_3 represents the nonradiative recombination energy loss from direct measurement of the EQE of electroluminescence (EQE_{EL}) of OSCs. The detailed E_{loss} data are summarized in Table 2, and further measurements can be found in the Supporting Information (Section 7, Figure S9, and Table S10). As shown in Table 2, the variation in the central core structure has a marginal impact on ΔE_1 in the optimized OSC devices. ΔE_2 , caused by radiative recombination below the bandgap, can be effectively reduced by narrowing the energy level gap between the donor and acceptor. Therefore, CH-iBQ-based OSCs displayed a higher ΔE_2 of 0.106 eV compared to CH-BQ (0.096 eV), mainly owing to its deeper HOMO energy level. Surprisingly, CH-BBQ-based devices exhibited a comparable ΔE_2 (0.105 eV) with CH-iBQ despite

having the deepest HOMO energy level. The ΔE_3 values, calculated using two different methods, showed a similar trend for the binary OSCs. As plotted in Figure 3e, PM6:CH-iBQ binary device yields the highest EQE_{EL} of 1.42×10^{-4} , leading to the smallest ΔE_3 . Conversely, the PM6:CH-BQ binary exhibited the largest ΔE_3 owing to its lowest EQE_{EL} of 0.28×10^{-4} . Finally, the total E_{loss} can be quantified, which are 0.602, 0.550, and 0.567 eV for CH-BQ-, CH-iBQ-, and CH-BBQ-based binary devices, respectively (Figure 3d). Besides, considering the importance of device lifespan, the thermal stability of OSCs was preliminarily investigated. After heating all devices at 65 °C for 200 h, the PCEs of CH-BQ-, CH-iBQ-, and CH-BBQ-based binary OSCs dropped to 75.5%, 76.5%, and 81.3% of their initial PCEs, respectively (Figure 3f).

Table 2. The distributions of total energy loss in solar cells based on the SQ limit theory.

BHJs	E_g^{PV} (eV)	V_{OC}^{SQ} (V)	ΔE_1 (eV)	V_{OC}^{rad} (V)	ΔE_2 (eV)	$\Delta E_3^{[a]}$ (eV)	$\Delta E_3^{[b]}$ (eV)	V_{OC} (V)	E_{loss} (eV)
PM6/CH-BQ	1.442	1.175	0.267	1.079	0.096	0.239	0.269	0.840	0.602
PM6/CH-iBQ	1.429	1.163	0.266	1.057	0.106	0.178	0.228	0.879	0.550
PM6/CH-BBQ	1.448	1.181	0.267	1.076	0.105	0.195	0.242	0.881	0.567

[a] Calculated from V_{OC}^{rad} through the equation of $\Delta E_3 = qV_{OC}^{rad} - qV_{OC}$; [b] Calculated from EQE_{EL} through the equation of $\Delta E_3 = -kT \ln(\text{EQE}_{EL})$.

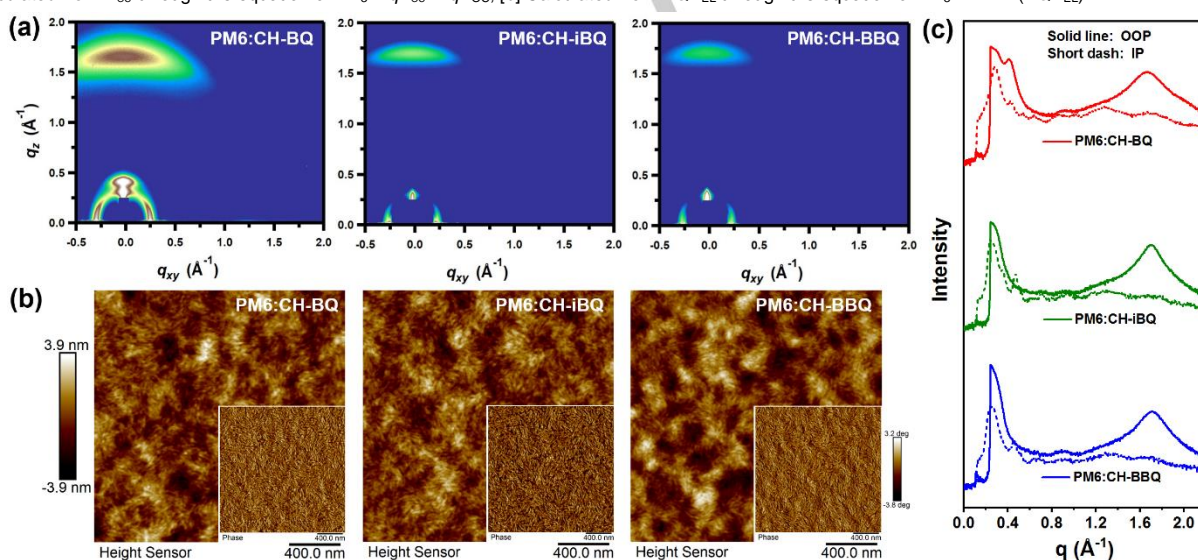


Figure 4. Morphology characterization of relevant blend films. a) 2D grazing-incidence wide-angle X-ray scattering patterns and b) Atomic force microscopy height/phase images of blend films; c) In-plane and out-of-plane line-cut profiles of blend films.

The abovementioned results indicate the influence of different electron-deficient cores on the photovoltaic properties of the three NFAs. To explain the intrinsic mechanism of the three NFAs, we investigated their charge carrier dynamics and morphology and conducted molecular simulation. First, charge carrier dynamics in the OSCs were investigated in various ways. As displayed in Figure 3c, CH-BQ-based OSCs suffered mediocre exciton dissociation efficiency (η_{diss} , 93.9%) and charge collection efficiency (η_{coll} , 75.0%), while CH-iBQ- and CH-BBQ-based OSCs showed much-enhanced η_{diss} (over 98%) and η_{coll} (over 89%), contributing to improved J_{SC} and EQE. The improved η_{diss} correlated positively with the downshifted HOMO energy

levels of CH-iBQ and CH-BBQ, strengthening the driving force for exciton dissociation^[20]. Enhanced η_{coll} is usually attributed to the high hole and electron mobilities (μ_h and μ_e , respectively) and well balanced μ_h/μ_e ratios of BHJ blends^[21]. As expected, PM6:CH-BQ blends exhibited μ_h and μ_e of 8.33×10^{-4} and 2.87×10^{-4} $\text{cm}^2 \cdot \text{V}^{-1} \cdot \text{s}^{-1}$, respectively, affording a μ_h/μ_e ratio of 2.90, while PM6:CH-iBQ and PM6:CH-BBQ blends showed enhanced μ_h and μ_e ($10.3 \times 10^{-4}/4.13 \times 10^{-4}$ and $12.3 \times 10^{-4}/4.98 \times 10^{-4}$ $\text{cm}^2 \cdot \text{V}^{-1} \cdot \text{s}^{-1}$, respectively) and well balanced μ_h/μ_e ratios (2.49 and 2.47, respectively) (Figure S10 and Table S11). In OSCs, bimolecular recombination and trap-assisted recombination are the two major charge recombination channels that would result in the loss of FFs

and PCEs. Analysis of the dependence of J_{SC} and V_{OC} on light intensity indicated that the bimolecular recombination is unlikely to have a major impact on all three binary OSCs, while CH-iBQ- and CH-BBQ-based OSCs suffered less trap-assisted recombination than CH-BQ-based devices (Figure S11 and Table S12). In addition, transient photocurrent/photovoltage characterizations were performed to quantitatively analyze charge recombination and extraction in the devices. As shown in Figure S12, CH-BBQ-based OSCs displayed more efficient charge extraction (0.45 μ s) and longer carrier lifetime (18.25 μ s) compared to CH-BQ and CH-iBQ. It is noteworthy that for the ternary system of PM6:CH-BBQ:BO-4Cl, it not only exhibited essentially enhanced μ_h and μ_e (23.0×10^{-4} and 13.7×10^{-4} $\text{cm}^2 \cdot \text{V}^{-1} \cdot \text{s}^{-1}$, respectively) along with more balanced μ_h/μ_e ratio (1.68) (Figure S10 and Table S11), but also displayed improved charge extraction (0.39 μ s) and prolonged carrier lifetime (23.85 μ s) as compared with binary systems (Figure S12), which coincide well with its high PCE value.

Film morphology is crucial in achieving favorable charge carrier dynamics and PCE records in OSCs. Therefore, the grazing-incidence wide-angle X-ray scattering technique was employed to probe molecular packing behaviors in thin films. As displayed in Figure S13, all the neat films of PM6 and acceptors exhibited an evident (010) peak along the out-of-plane (OOP) direction at 1.62–1.70 \AA^{-1} , corresponding to a π – π stacking distance of 3.68–3.87 \AA , suggesting a face-on orientation that favors charge transport^[22]. Meanwhile, the increased coherence lengths (CLs) demonstrated the sequentially enhanced crystallinity of the acceptors in the OOP direction of the three NFAs. Compared with CH-BQ (CL of 29.9 \AA), the film of CH-iBQ and CH-BBQ showed an increase of 44% (43.2 \AA) and 97% (58.9 \AA) in CL, respectively (Figure S14 and Table S13). In the donor and acceptor (D:A) blends, the d -spacings and corresponding CLs of (010) peak were estimated to be 3.76 and 27.6 \AA for PM6:CH-BQ, 3.70 and 37.4 \AA for PM6:CH-iBQ, and 3.67 and 31.1 \AA for PM6:CH-BBQ (Figure 4a and 4c, Table S14). Thus, PM6:CH-iBQ and PM6:CH-BBQ blends exhibited shorter d -spacings and larger CLs along the OOP direction compared to PM6:CH-BQ, which would facilitate the charge extraction/transport and boost the FF and J_{SC} of the devices. These results coincide well with the enhanced charge carrier mobilities and improved η_{coll} of PM6:CH-iBQ and PM6:CH-BBQ binaries. Compared to CH-BQ, the more ordered intermolecular packing and better crystallinity of CH-iBQ- and CH-BBQ-based films is highly correlated with their horizontally extended electron-deficient central core: the more the central core extended, the more crystalline the film becomes. Atomic force microscopy (AFM) was conducted to observe the phase separation of the active layers. The AFM images (Figure 4b) illustrate that all blend films present a fiber-like uniform surface and well-defined phase separation. The root mean square (RMS) roughness of PM6:CH-BQ, PM6:CH-iBQ, and PM6:CH-BBQ are 0.98, 0.92, and 1.10 nm, respectively. Compared to others, the slightly higher RMS of PM6:CH-BQ is probably caused by the inferior miscibility between CH-BQ and PM6 donor, as evaluated by their Flory–Huggins interaction parameter (χ)^[23] (0.0255, 0.0131, and 0.0151 for CH-BQ-, CH-iBQ-, and CH-BBQ-based blends, respectively, see Figure S15 and Table S15 for the details).

Experimental results indicate that the structure of the central electron-deficient core considerably impacts charge carrier transport and morphological characteristics in OSCs. However, certain questions remain unanswered: Why does CH-BQ have a unique electron configuration and the lowest bandgap? Why do horizontally extended acceptors (CH-iBQ and CH-BBQ) exhibit superior photovoltaic performance compared to the vertically extended CH-BQ? For an in-depth study on how the electron configuration of the electron-deficient central core of acceptors causes substantial differences and to shed light on further molecular optimization of NFAs, theoretical calculations were conducted to explore the electronic structure of the ground and excited state, as well as donor–acceptor (D–A) interactions at the molecular level.

Figure 5a shows the HOMO and LUMO energy levels obtained from DFT calculations for the three core fragments, indicating that the vertically extended one has the smallest HOMO–LUMO gap. This phenomenon can be explained by the annellation theory or Clar's model, where the HOMO–LUMO gap of a fragment is proportional to the number of aromatic π -sextets^[24]. Therefore, the linear core has the smallest gap and is more likely to participate in the frontier orbital of the molecule, leading to a reduced bandgap of the entire molecule. Another theoretical approach for the reduced bandgap of CH-BQ is the symmetry matching of the fragment orbitals. As shown in Figures 5b and S4, the three NFA molecules were disintegrated into two fragments: the core and the base. For CH-BQ, the HOMO of the core fragment is anti-symmetric (AS), while the LUMO is symmetric (S). The HOMO/LUMO orbitals of the base fragment have the same symmetry, enabling HOMO–HOMO and LUMO–LUMO interactions and disabling HOMO–LUMO interactions between the core and base fragments. This promotes the HOMO/LUMO contributions of the core fragment to the overall molecular HOMO/LUMO, reducing the HOMO–LUMO gap of the entire molecule. In contrast, for CH-iBQ, the frontier orbitals of core fragments cannot effectively match the base fragment, leading to prohibited participation of the core fragment in the HOMO–LUMO distribution and widened bandgap. Similarly, in CH-BBQ, although LUMO orbitals of the fragment symmetrically match with that of the top fragment, the energy levels of LUMO in the top and base fragments differ substantially, leading to a similar situation as CH-iBQ. In addition, the LUMO distribution of the base fragment is minimal at the connecting point, further reducing the contribution of the LUMO of the top fragment to the LUMO of the whole molecule (Figure S4)^[25].

Furthermore, the interaction of PM6 and the three acceptors in BHJ was simulated using MD (Figure 5c). The simulation system contained 15 PM6 octamers and 90 acceptor molecules. The GAFF2 force field parameters were used, and the equilibrium bond length, bond angle, and dihedral angle parameters were optimized using ztp^[26]. Five independent trajectories were produced for each system, and the last 10 ns (50 frames) of each production trajectory were analyzed. Close contacts of the non-alkyl chain heavy atoms were analyzed (see Section 13 in ESI for detail), and the results showed no visible difference between the three acceptors. The number of close contacts involving the donor fragment of CH-BBQ was slightly higher than that of CH-iBQ and CH-BQ, which is expected because of the larger core area in CH-BBQ.

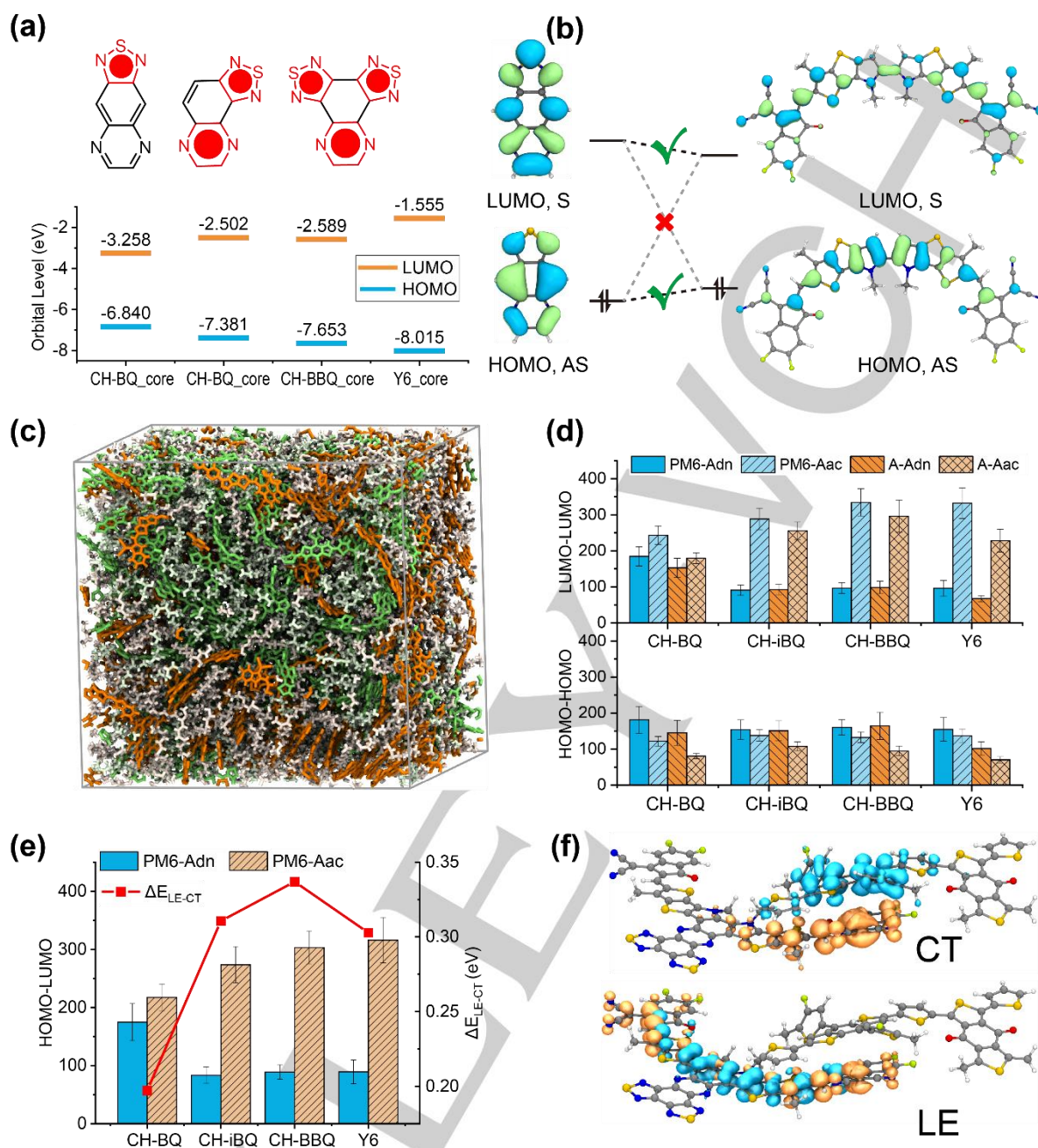


Figure 5. a) Upper figure illustrates Clar's model with aromatic π -sextets highlighted in red circles. Lower figure below shows the HOMO/LUMO energy levels of the core fragment. b) Frontier orbitals of the core and base fragments of CH-BQ, as well as their interactions. The letter 'S' represents symmetric, while 'AS' represents anti-symmetric. c) A snapshot from MD simulation, where green represents PM6 molecules, orange represents CH-BQ molecules, and white represents alkyl chains. d) The interaction strengths of the frontier orbitals between the molecules obtained through statistical analysis from the MD trajectory. The upper/lower figures represent the LUMO-LUMO/HOMO-HOMO interaction strengths, respectively. In the figures, "A" represents the acceptor molecules, while Adn and Aac represent the donor and acceptor fragments of the acceptor molecule types, respectively. e) The left Y-axis shows the HOMO-LUMO interaction strengths between the donor and acceptor fragment. The right Y-axis displays the energy difference between the local excited (LE) and charge transfer (CT) states in the complex formed by the acceptor and PM6. f) A representative hole-electron distribution of the LE/CT state in a PM6:CH-BBQ complex.

Another calculation was processed to quantify the strength of the orbital interactions between the fragments, considering the distribution of frontier orbitals on each atom and their contact distances. The HOMO-HOMO and LUMO-LUMO interaction strengths, shown in Figure 5d, represent the hole and electron transport pathways, respectively, and the corresponding charge

separation pathway. For all three acceptors, their HOMO-HOMO interaction profile showed a similar pattern, with the donor fragment of the acceptor (Adn) being more involved in the HOMO interaction than its acceptor fragment (Aac) (Figure S16), indicating a higher likelihood of charge separation owing to hole transfer when the donor fragment of the acceptor is in contact with

PM6. However, the LUMO–LUMO interactions of all three acceptors showed considerable differences. The Adn of CH-BQ was more involved in LUMO interactions than other acceptors owing to the larger electron distribution of LUMO on its central core. This means that the hole and electron transport pathways in CH-BQ may have more spatial overlap compared to the other two, leading to increased charge recombination in CH-BQ-based devices, consistent with the experimental results^[27]. Similarly, the interactions between the donor HOMO and acceptor LUMO were quantified and shown in Figure 5e, representing the charge recombination pathway at the donor–acceptor interface. Charge transfer between CH-BQ and PM6 mainly occurred on the donor fragment of CH-BQ, indicating the simultaneous opening of the charge separation pathway due to the HOMO–HOMO interaction and the charge recombination pathway owing to the HOMO–LUMO interaction when the donor fragment of CH-BQ comes into contact with PM6 (Figure S18 and Table S16)^[28].

The charge recombination tendency is also analyzed thermodynamically. The red line shown in Figure 5e represents the energy difference between the local excited (LE) and charge transfer (CT) states (see Table S4 for detail). The hole–electron distribution of the LE and CT states for a D–A complexes is shown in Figures 5f and S6. The lowest energy LE state shows hole–electron distribution on the acceptor, while the lowest energy CT state exhibits complete hole–electron separation. Therefore, a smaller energy gap between the LE and CT states implies a higher likelihood of charge recombination. Compared to the other two acceptors, CH-BQ has a stronger charge recombination tendency owing to its smaller energy gap between the LE and CT states, mainly attributed to its smaller HOMO–LUMO gap and larger HOMO–LUMO overlap.

Overall, the results of the computational approach indicate the substantial impact of the electron configuration of the central core on the energy levels and hole/electron distribution of NFA molecule and play a decisive role in D–A intermolecular interaction, charge carrier dynamics, and device performance. The electron-deficient core extension strategy can be a double-edged sword, meaning that inappropriate design might sabotage the device performance. The combination of DFT calculation and MD simulation provides a useful tool for structure–property prediction and offers some inspiration for solving this conundrum.

Conclusion

A new set of NFAs with extended electron-deficient central cores was developed for OSC devices. Each central core imparted distinct physicochemical properties and electronic configurations to the acceptors, leading to a demarcated photovoltaic performance in OSC devices. The vertically extended acceptor, CH-BQ, exhibited red-shifted absorption but yielded a lower PCE of 12.85% with three dissatisfactory parameters owing to its high-lying energy levels, poor exciton disassociation/charge collection efficiency, unsatisfactory charge recombination along with mediocre crystallinity and intermolecular packing. In contrast, horizontally extended acceptors, CH-iBQ and CH-BBQ, displayed a narrower range of light-harvesting but demonstrated suitable energy levels, enhanced crystallinity, and well-controlled charge carrier dynamics in devices, leading to satisfactory V_{oc} and FF, giving out a PCE of 17.97% and 18.19%, respectively. Remarkable, CH-BBQ, when combined with NFA BO-4Cl in a

ternary OSC, achieved a PCE of 18.94% with V_{oc} of 0.882 V, J_{sc} of 27.05 mA·cm⁻², and FF of 79.4%. In addition, computational simulations indicated that only a central core with an appropriate electron configuration positively affected energy levels, hole/electron distribution, and D–A intermolecular interactions, resulting in satisfactory device performance. Conversely, an improperly designed central core extension strategy could be counterproductive for OSCs. This study not only highlights a new pathway in the structure modification of NFAs and the effectiveness of central cores for boosting the PCEs of OSCs but also provides experimental and computational guidelines for developing high-performance NFAs.

Acknowledgements

The authors gratefully acknowledge the financial support from MoST (2022YFB4200400, 2019YFA0705900) and NSFC (21935007, 52025033, 52303237, 51873160) of China, Youth Innovation Promotion Association CAS (No.2019373), Tianjin City (20JCZDJC00740), 111 Project (B12015), Natural Science Foundation of Chongqing (CSTB2023NSCQ-MSX0268), the 100 Young Academic Leaders Program of Nankai University (020-ZB22000110), the Fundamental Research Funds for the Central Universities, Nankai University (023-ZB22000105), and Haihe Laboratory of Sustainable Chemical Transformations.

Conflict of interest

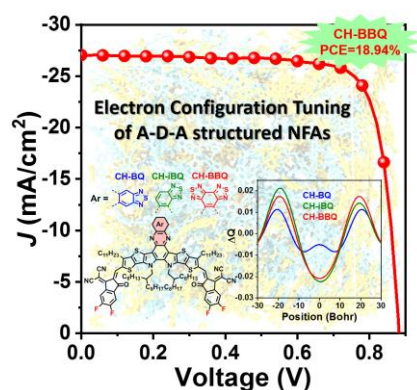
The authors declare no conflict of interest.

Keywords: Electronic Configuration Tuning · Electron-deficient Central Core · Non-Fullerene Acceptor · Organic Solar Cells · Molecular Dynamics Simulations.

- [1] a) L. Dou, Y. Liu, Z. Hong, G. Li, Y. Yang, *Chem. Rev.* **2015**, *115*, 12633–12665; b) L. Lu, T. Zheng, Q. Wu, A. M. Schneider, D. Zhao, L. Yu, *Chem. Rev.* **2015**, *115*, 12666–12731; c) T. Duan, Q. Chen, D. Hu, J. Lv, D. Yu, G. Li, S. Lu, *Trends Chem.* **2022**, *4*, 773–791; d) Y. Huang, E. J. Kramer, A. J. Heeger, G. C. Bazan, *Chem. Rev.* **2014**, *114*, 7006–7043.
- [2] a) H. Chen, H. Liang, Z. Guo, Y. Zhu, Z. Zhang, Z. Li, X. Cao, H. Wang, W. Feng, Y. Zou, L. Meng, X. Xu, B. Kan, C. Li, Z. Yao, X. Wan, Z. Ma, Y. Chen, *Angew. Chem. Int. Ed.* **2022**, *61*, e202209580; b) L. Zhan, S. Li, Y. Li, R. Sun, J. Min, Y. Chen, J. Fang, C. Q. Ma, G. Zhou, H. Zhu, L. Zuo, H. Qiu, S. Yin, H. Chen, *Adv. Energy Mater.* **2022**, *12*, 2201076; c) Y. Zou, H. Chen, X. Bi, X. Xu, H. Wang, M. Lin, Z. Ma, M. Zhang, C. Li, X. Wan, G. Long, Y. Zhaoyang, Y. Chen, *Energy Environ. Sci.* **2022**, *15*, 3519–3533; d) F. Meng, Y. Qin, Y. Zheng, Z. Zhao, Y. Sun, Y. Yang, K. Gao, D. Zhao, *Angew. Chem. Int. Ed.* **2023**, *62*, e202217173; e) H. Zhuo, X. Li, J. Zhang, S. Qin, J. Guo, R. Zhou, X. Jiang, X. Wu, Z. Chen, J. Li, L. Meng, Y. Li, *Angew. Chem. Int. Ed.* **2023**, e202303551; f) Z. Zheng, J. Wang, P. Bi, J. Ren, Y. Wang, Y. Yang, X. Liu, S. Zhang, J. Hou, *Joule* **2022**, *6*, 171–184; g) K. Liu, Y. Jiang, F. Liu, G. Ran, F. Huang, W. Wang, W. Zhang, C. Zhang, J. Hou, X. Zhu, *Adv. Mater.* **2023**, *35*, 2300363; h) F. Liu, L. Zhou, W. Liu, Z. Zhou, Q. Yue, W. Zheng, R. Sun, W. Liu, S. Xu, H. Fan, L. Feng, Y. Yi, W. Zhang, X. Zhu, *Adv. Mater.* **2021**, *33*, 2100830; i) Z. Zhou, W. Liu, G. Zhou, M. Zhang, D. Qian, J. Zhang, S. Chen, S. Xu, C. Yang, F. Gao, H. Zhu, F. Liu, X. Zhu, *Adv.*

- Mater.* **2020**, *32*, 1906324; j) Z. Chen, J. Zhu, D. Yang, W. Song, J. Shi, J. Ge, Y. Guo, X. Tong, F. Chen, Z. Ge, *Energy Environ. Sci.* **2023**, *16*, 3119-3127.
- [3] a) Y. Wei, Z. Chen, G. Lu, N. Yu, C. Li, J. Gao, X. Gu, X. Hao, G. Lu, Z. Tang, J. Zhang, Z. Wei, X. Zhang, H. Huang, *Adv. Mater.* **2022**, *34*, 2204718; b) L. Zhu, M. Zhang, J. Xu, C. Li, J. Yan, G. Zhou, W. Zhong, T. Hao, J. Song, X. Xue, Z. Zhou, R. Zeng, H. Zhu, C. C. Chen, R. C. I. MacKenzie, Y. Zou, J. Nelson, Y. Zhang, Y. Sun, F. Liu, *Nat. Mater.* **2022**, *21*, 656-663; c) J. Fu, P. W. K. Fong, H. Liu, C. S. Huang, X. Lu, S. Lu, M. Abdelsamie, T. Kodalle, C. M. Sutter-Fella, Y. Yang, G. Li, *Nat. Commun.* **2023**, *14*, 1760.
- [4] Y. Lin, J. Wang, Z. G. Zhang, H. Bai, Y. Li, D. Zhu, X. Zhan, *Adv. Mater.* **2015**, *27*, 1170-1174.
- [5] a) H. Chen, Z. Zhang, P. Wang, Y. Zhang, K. Ma, Y. Lin, T. Duan, T. He, Z. Ma, G. Long, C. Li, B. Kan, Z. Yao, X. Wan, Y. Chen, *Energy Environ. Sci.* **2023**, *16*, 1773-1782; b) L. Meng, Y. Zhang, X. Wan, C. Li, X. Zhang, Y. Wang, X. Ke, Z. Xiao, L. Ding, R. Xia, H.-L. Yip, Y. Cao, Y. Chen, *Science*. **2018**, *361*, 1094-1098; c) J. Wang, Z. Zheng, P. Bi, Z. Chen, Y. Wang, X. Liu, S. Zhang, X. Hao, M. Zhang, Y. Li, J. Hou, *Nat. Sci. Rev.* **2023**, nwad085.
- [6] a) J. Yuan, Y. Zhang, L. Zhou, G. Zhang, H.-L. Yip, T.-K. Lau, X. Lu, C. Zhu, H. Peng, P. A. Johnson, M. Leclerc, Y. Cao, J. Ulanski, Y. Li, Y. Zou, *Joule*. **2019**, *3*, 1140-1151; b) H. Chen, Y. Zou, H. Liang, T. He, X. Xu, Y. Zhang, Z. Ma, J. Wang, M. Zhang, Q. Li, C. Li, G. Long, X. Wan, Z. Yao, Y. Chen, *Sci. Chi. Chem.* **2022**, *65*, 1362-1373; c) L. Meng, H. Liang, G. Song, M. Li, Y. Huang, C. Jiang, K. Zhang, F. Huang, Z. Yao, C. Li, X. Wan, Y. Chen, *Sci. Chi. Chem.* **2023**, *66*, 808-815.
- [7] G. Zhang, X.-K. Chen, J. Xiao, P. C. Y. Chow, M. Ren, G. Kupgan, X. Jiao, C. C. S. Chan, X. Du, R. Xia, Z. Chen, J. Yuan, Y. Zhang, S. Zhang, Y. Liu, Y. Zou, H. Yan, K. S. Wong, V. Coropceanu, N. Li, C. J. Brabec, J.-L. Bredas, H.-L. Yip, Y. Cao, *Nat. Commun.* **2020**, *11*, 3943.
- [8] Y. Shi, L. Zhu, Y. Yan, M. Xie, G. Liang, J. Qiao, J. Zhang, X. Hao, K. Lu, Z. Wei, *Adv. Energy Mater.* **2023**, *13*, 2300458.
- [9] a) Y. Cui, P. Zhu, X. Liao, Y. Chen, *J. Mater. Chem. C* **2020**, *8*, 15920-15939; b) V. B. R. Pedersen, S. K. Pedersen, Z. Jin, N. Kofod, B. W. Laursen, G. V. Baryshnikov, C. Nuckolls, M. Pittelkow, *Angew. Chem. Int. Ed.* **2022**, *61*, e202212293.
- [10] a) F. Eisner, J. Nelson, *Joule*. **2021**, *5*, 1319-1322; b) C. Poelking, D. Andrienko, *J. Am. Chem. Soc.* **2015**, *137*, 6320-6326; c) R. Yu, H. Yao, Y. Xu, J. Li, L. Hong, T. Zhang, Y. Cui, Z. Peng, M. Gao, L. Ye, Z. a. Tan, J. Hou, *Adv. Funct. Mater.* **2021**, *31*, 2010535; d) S. Karuthedath, J. Gorenflot, Y. Firdaus, N. Chaturvedi, C. S. P. De Castro, G. T. Harrison, J. I. Khan, A. Markina, A. H. Balawi, T. A. D. Peña, W. Liu, R.-Z. Liang, A. Sharma, S. H. K. Paleti, W. Zhang, Y. Lin, E. Alarousu, S. Lopatin, D. H. Anjum, P. M. Beaujuge, S. De Wolf, I. McCulloch, T. D. Anthopoulos, D. Baran, D. Andrienko, F. Laquai, *Nat. Mater.* **2021**, *20*, 378-384; e) L. Perdigón-Toro, H. Zhang, A. Markina, J. Yuan, S. M. Hosseini, C. M. Wolff, G. Zuo, M. Stolterfoht, Y. Zou, F. Gao, D. Andrienko, S. Shoaee, D. Neher, *Adv. Mater.* **2020**, *32*, 1906763.
- [11] a) T. Xu, J. Lv, K. Yang, Y. He, Q. Yang, H. Chen, Q. Chen, Z. Liao, Z. Kan, T. Duan, K. Sun, J. Ouyang, S. Lu, *Energy Environ. Sci.* **2021**, *14*, 5366-5376; b) Y. Cho, Z. Sun, K. M. Lee, G. Zeng, S. Jeong, S. Yang, J. E. Lee, B. Lee, S.-H. Kang, Y. Li, Y. Li, S. K. Kwak, C. Yang, *ACS Energy Lett.* **2022**, *8*, 96-106; c) L. Zhang, X. Zhu, D. Deng, Z. Wang, Z. Zhang, Y. Li, J. Zhang, K. Lv, L. Liu, X. Zhang, H. Zhou, H. Ade, Z. Wei, *Adv. Mater.* **2022**, *34*, e2106316; d) L. Guo, Q. Li, J. Ren, Y. Xu, J. Zhang, K. Zhang, Y. Cai, S. Liu, F. Huang, *Energy Environ. Sci.* **2022**, *15*, 5137-5148.
- [12] Y. Shi, Y. Chang, K. Lu, Z. Chen, J. Zhang, Y. Yan, D. Qiu, Y. Liu, M. A. Adil, W. Ma, X. Hao, L. Zhu, Z. Wei, *Nat. Commun.* **2022**, *13*, 3256.
- [13] X. Wang, C. Feng, P. Liu, Z. He, Y. Cao, *Small*. **2022**, *18*, 2107106.
- [14] X. Wan, C. Li, M. Zhang, Y. Chen, *Chem. Soc. Rev.* **2020**, *49*, 2828-2842.
- [15] F. Opoku, K. K. Govender, C. G. C. E. van Sittert, P. P. Govender, *Int. J. Quantum Chem.* **2018**, *118*, e25505.
- [16] a) X. Song, H. Yu, X. Yan, Y. Zhang, Y. Miao, K. Ye, Y. Wang, *Dalton Trans.* **2018**, *47*, 6146-6155; b) A. P. Komin, M. Carmack, *J. Heterocycl. Chem.* **1975**, *12*, 829-833.
- [17] T. J. Wen, Z. X. Liu, Z. Chen, J. Zhou, Z. Shen, Y. Xiao, X. Lu, Z. Xie, H. Zhu, C. Z. Li, H. Chen, *Angew. Chem. Int. Ed. Engl.* **2021**, *60*, 12964-12970.
- [18] Y. Wang, D. Qian, Y. Cui, H. Zhang, J. Hou, K. Vandewal, T. Kirchartz, F. Gao, *Adv. Energy Mater.* **2018**, *8*, 1801352.
- [19] a) J. Yao, T. Kirchartz, M. S. Vezie, M. A. Faist, W. Gong, Z. He, H. Wu, J. Troughton, T. Watson, D. Bryant, J. Nelson, *Phys. Rev. Appl.* **2015**, *4*, 014020; b) J. Liu, S. Chen, D. Qian, B. Gautam, G. Yang, J. Zhao, J. Bergqvist, F. Zhang, W. Ma, H. Ade, O. Inganäs, K. Gundogdu, F. Gao, H. Yan, *Nat. Energy*. **2016**, *1*, 16089.
- [20] D. Qiu, J. Zhang, K. Lu, Z. Wei, *Nano Res.* **2023**, doi: 10.1007/s12274-023-5723-x.
- [21] X. Zhang, C. Li, J. Xu, R. Wang, J. Song, H. Zhang, Y. Li, Y.-N. Jing, S. Li, G. Wu, J. Zhou, X. Li, Y. Zhang, X. Li, J. Zhang, C. Zhang, H. Zhou, Y. Sun, Y. Zhang, *Joule*. **2022**, *6*, 444-457.
- [22] A. Hexemer, W. Bras, J. Glossinger, E. Schaible, E. Gann, R. Kirian, A. MacDowell, M. Church, B. Rude, H. Padmore, *J. Phys.: Conf. Ser.* **2010**, *247*, 012007.
- [23] S. Nilsson, A. Bernasik, A. Budkowski, E. Moons, *Macromolecules*. **2007**, *40*, 8291-8301.
- [24] J. O. Oña-Ruales, Y. Ruiz-Morales, *J. Phys. Chem. A*. **2014**, *118*, 5212-5227.
- [25] R. G. Pearson, in *New Concepts I*, Springer Berlin Heidelberg, Berlin, Heidelberg, **1973**, pp. 75-112.
- [26] OSChina Corp. <https://gitee.com/coordmagic/coordmagic>.
- [27] J. Terao, A. Wadahama, A. Matono, T. Tada, S. Watanabe, S. Seki, T. Fujihara, Y. Tsuji, *Nat. Commun.* **2013**, *4*, 1691.
- [28] P. O. J. Scherer, S. F. Fischer, in *Theoretical Molecular Biophysics*, Springer Berlin Heidelberg, Berlin, Heidelberg, **2017**, pp. 201-224.

Entry for the Table of Contents



A series of acceptors featuring conjugation-extended electron-deficient cores were synthesized via a newly developed strategy for organic solar cells, and power conversion efficiencies (PCEs) of up to ~19% were achieved. The properties of new acceptors were systematically investigated and elucidated experimentally and computationally.